Joule

Article

High-emissivity, thermally robust emitters for high power density thermophotovoltaics

Graphical abstract

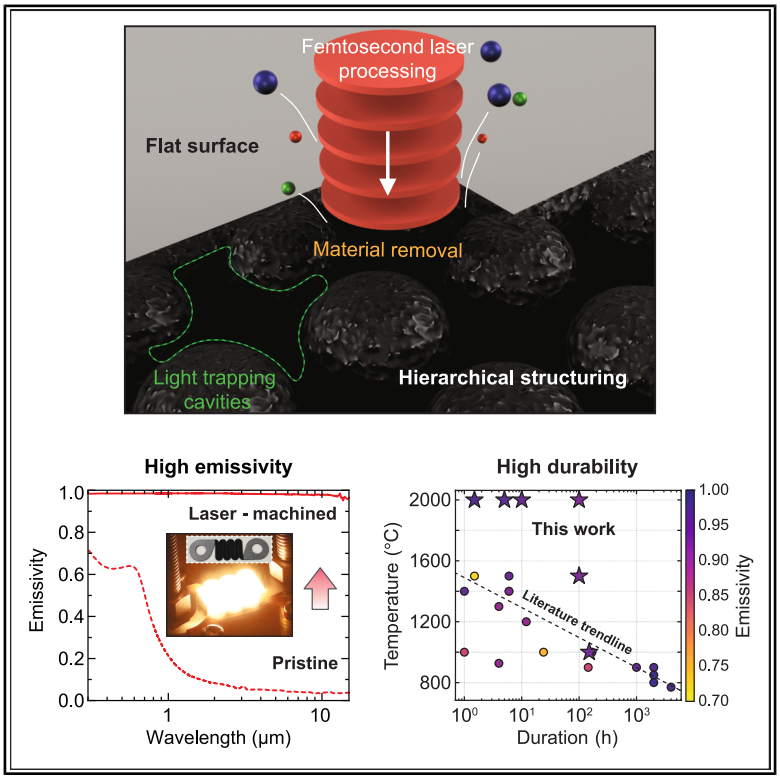

Highlights

- Femtosecond laser processing creates near-blackbody surfaces on diverse materials
- Laser-blackened surfaces (LaBS) show high emissivity across broad wavelengths
- LaBS double thermophotovoltaic power output while maintaining high efficiency
- LaBS retain high emissivity after 100+ h above 1,500°C

Authors

Minok Park, Shomik Verma, Alina LaPotin, ..., Sean D. Lubner, Costas P. Grigoropoulos, Vassilia Zorba

Correspondence

ase@mit.edu (A.H.), slubner@bu.edu (S.D.L.), cgrigoro@berkeley.edu (C.P.G.), vzorba@lbl.gov (V.Z.)

In brief

Thermophotovoltaic and solar thermal systems require emitters with high emissivity and durability at extreme temperatures. This work uses femtosecond laser processing to create light-trapping micro/nanostructures on various material surfaces. The surfaces exhibit high broadband emissivity and remain stable at high temperatures. The resulting emitters demonstrate doubling of thermophotovoltaic power output without compromising efficiency. This scalable, nearly material-agnostic approach offers a promising pathway for advancing performance in high-temperature energy applications through durable surface structuring.

Park et al., 2025, Joule 9, 102005
July 16, 2025
https://doi.org/10.1016/j.joule.2025.102005

CellPress

Please cite this article in press as: Park et al., High-emissivity, thermally robust emitters for high power density thermophotovoltaics, Joule (2025), https://doi.org/10.1016/j.joule.2025.102005

Joule

CellPress

Article

High-emissivity, thermally robust emitters for high power density thermophotovoltaics

Minok Park,[1,2,3,7] Shomik Verma,[4,7] Alina LaPotin,[4] Dustin P. Nizamian,[5] Ravi Prasher,[1,2] Asegun Henry,[4,*] Sean D. Lubner,[1,6,*] Costas P. Grigoropoulos,[1,2,*] and Vassilia Zorba[1,2,8,*]

[1]Energy Technologies Area, Lawrence Berkeley National Laboratory, Berkeley, CA 94720, USA
[2]Department of Mechanical Engineering, University of California at Berkeley, Berkeley, CA 94720, USA
[3]Department of Mechanical and Automotive Engineering, Kongju National University, Cheonan 31080, Republic of Korea
[4]Department of Mechanical Engineering, Massachusetts Institute of Technology, Cambridge, MA 02139, USA
[5]Antora Energy, Inc., Sunnyvale, CA 94089, USA
[6]Department of Mechanical Engineering, Division of Materials Science and Engineering, Boston University, Boston, MA 02215, USA
[7]These authors contributed equally
[8]Lead contact
*Correspondence: ase@mit.edu (A.H.), slubner@bu.edu (S.D.L.), cgrigoro@berkeley.edu (C.P.G.), vzorba@lbl.gov (V.Z.)
https://doi.org/10.1016/j.joule.2025.102005

CONTEXT & SCALE Thermal radiation—the emission of heat as light—is essential for technologies such as thermophotovoltaics (TPVs) and solar thermal systems. However, many high-temperature materials emit low thermal radiation, limiting system performance. We use laser processing to engineer the surfaces of diverse materials into near-black emitters that radiate heat efficiently across a broad spectrum. This is achieved by creating complex micro- and nanoscale surface structures that trap light without changing the material's bulk properties. The resulting laser-blackened surfaces (LaBS) show record-high emissivity (>0.96) and maintain high emissivity after 100+ h at elevated temperatures (>1,500°C). When integrated into TPV systems, LaBS nearly double electrical power output while maintaining high conversion efficiency. This scalable, coating-free, and versatile approach opens new opportunities for improving performance in high-temperature energy applications.

SUMMARY

Thermal radiative energy transport is essential for high-temperature energy harvesting technologies, including thermophotovoltaics (TPVs) and grid-scale thermal energy storage. However, the inherently low emissivity of conventional high-temperature materials constrains radiative energy transfer, thereby limiting system performance and technoeconomic viability. Here, we demonstrate ultrafast femtosecond laser-material interactions to transform diverse materials into near-blackbody surfaces with broadband spectral emissivity above 0.96. This enhancement arises from hierarchically engineered light-trapping microstructures enriched with nanoscale features, effectively decoupling surface optical properties from bulk thermomechanical properties. These laser-blackened surfaces (LaBS) exhibit exceptional thermal stability, retaining high emissivity for over 100 h at temperatures exceeding 1,000°C, even in oxidizing environments. When applied as TPV thermal emitters, Ta LaBS double electrical power output from 2.19 to 4.10 W cm^{-2} at 2,200°C while sustaining TPV conversion efficiencies above 30%. This versatile, largely material-independent technique offers a scalable and economically viable pathway to enhance emissivity for advanced thermal energy applications.

INTRODUCTION

High emissivity in the visible to infrared (IR) spectral range is crucial for effective thermal energy transport in solar and high-temperature energy applications, including thermophotovoltaics (TPVs),[1–3] concentrating solar power (CSP),[4,5] spacecraft thermal management,[6,7] and solar water desalination.[8–10] In these systems, low-emissivity materials can significantly limit a system's performance and economic viability, necessitating larger surface areas and increasing material and infrastructure costs.[11–13] Improving emissivity could thus have transformative effects on technologies that depend on thermal radiative energy transfer, especially in TPVs where enhanced power density and reduced system size could facilitate grid-scale thermal energy storage (TES) solutions that enable switching entirely to intermittent renewable energy.[14]

Please cite this article in press as: Park et al., High-emissivity, thermally robust emitters for high power density thermophotovoltaics, Joule (2025), https://doi.org/10.1016/j.joule.2025.102005

A blackbody (BB) is defined as a perfect absorber and therefore emitter across all wavelengths and for all directions, regardless of light polarization.[15–17] Hence, a BB has unity emissivity, maximizing thermal radiative energy transfer for a fixed surface area. Achieving this standard for TPV applications would substantially increase power density and reduce cost per power, which is often the dominant cost in TPV-based heat recovery and TES systems.[13]

Some conventional approaches for creating high-temperature broadband emitters use carbon-based materials with naturally high emissivities. However, these also have high vapor pressures that cause emitter sublimation and subsequent optically thick deposition onto the cooled TPV cells, rapidly degrading performance.[18,19] Another example, silicon carbide, can only be machined with diamond tipped tools.[20] Alternatively, lower vapor pressure non-carbon materials have been applied as coatings that achieve broadband absorption through geometric design, such as hierarchical structures, multilayer materials, or metamaterials.[21–24] However, these are prone to delamination and substrate compatibility challenges, such as from mismatched coefficients of thermal expansion or poor chemical adhesion, reducing practicality.[25]

Specifically for TPV systems utilizing back-surface reflectors, no contemporary emitter simultaneously satisfies the following five metrics: optical performance (defined in this work as broadband high emissivity), scalability to large areas, high-temperature stability, system integrability, and cost.[26] Refractory materials could be ideal candidates for TPV emitters as they offer thermal durability,[23] low vapor pressure,[18] and good machinability,[27] but they suffer from low intrinsic emissivities (e.g., tantalum [Ta] has an emissivity < 0.1 for wavelengths above 1 μm[28]). Decoupling these optical properties from the other metrics would significantly expand the viable design space, enabling the use of low vapor pressure and scalably machinable refractories. While this decoupling could in principle be accomplished via direct surface texturing, such approaches have thus far been limited to select materials and have not yet been demonstrated to produce significant and stable improvements to broadband emissivity at high temperatures.[29–33]

Ultrafast femtosecond (fs) laser ablation, which can induce surface material removal through rapid phase transformation,[16,34] has been widely used to alter surface structures for applications such as controlling wettability,[35,36] drilling and patterning,[37–39] structural surface coloration,[40,41] and bio-materials.[42,43] While fs laser processing has previously been used to create micro/nanoparticle-decorated structured surfaces with metal oxide layers and plasmon hybridizations to enhance light absorption and emissivity,[8,44] most efforts primarily focused on improving absorption within relatively narrow and specific spectral ranges (e.g., only up to the near-IR or solely in the mid-IR), while also frequently utilizing materials that are not suitable for high-temperature applications due to their low melting points (e.g., ~660°C for aluminum, Al).[45–49]

Here, we extend ultrafast fs laser ablation to more generally decouple surface broadband optical properties from thermomechanical stability across a variety of materials, creating persistent near-BB surfaces in high-temperature stable materials for TPV applications. A scalable fs laser ablation technique[50–52] is designed for fabrication of broadband high-emissivity, near-BB surfaces, termed laser-blackened surfaces (LaBS). We show that LaBS achieve near-unity spectral emissivity (>0.96) across 0.3–15 μm on different substrates, including refractory materials, primarily through the formation of light-trapping microstructures, effectively decoupling optical properties from bulk characteristics. As a result, high emissivity (~0.93) is maintained after heating to temperatures of 1,000°C in air and 1,500°C in argon (Ar). When used as a TPV thermal emitter from 1,700°C to 2,200°C, aTa LaBS achieves a 2-fold increase in generated electrical power compared with untreated Ta, which could significantly improve TES scalability by reducing system size and cost per Watt of delivered stored energy.

Beyond TPVs, this fs laser processing method offers a largely material-independent approach to enhancing high-temperature emissivity for a range of applications where different bulk material properties are required. By decoupling surface emissivity from bulk material properties, this approach opens new possibilities for economically viable, high-temperature radiative surfaces in the energy sector.

RESULTS AND DISCUSSION

Ultrafast fs laser-material interactions for fabricating microstructures with nanoscale features

Figure 1 describes the basis for enhanced light absorption to achieve near-BB surfaces. For a non-transparent, optically flat surface at the interface with the air (Figure 1A, top), the incident light is either reflected or absorbed as a function of complex refractive index (see details in Note S1).[15,16] Any deviation in the material's spectral refractive index from the ambient environment refractive index (1 for gas and vacuum) produces reflection and correspondingly yields emissivity lower than 1 for that wavelength. The spectral emissivity of metals in the IR regimes is typically low (i.e., they are of high reflectivity above 1-μm wavelength) because their dielectric functions increase with wavelength (and inversely decrease with respect to frequency). As a result, a flat metal surface cannot offer augmented thermal emission in the IR wavelength regime.

On the other hand, microstructured surfaces of multiscale texture and roughness can scatter and trap light within microcavities,[7,53] leading to enhanced light absorption (Figure 1A, bottom). To fabricate such surface morphologies, an ultrafast fs laser is employed for selective ablation of material from the surface, as depicted in Figures 1B, 1C, and S1A. Specifically, 500-fs laser pulses at a wavelength of 1,030 nm are focused on the target surface in ambient air. The incident laser power is fixed at 1.5 W with a repetition rate of 100 kHz and individual laser pulse fluences set to 2.1 J cm^{-2}. A total of 2,000 laser pulses are irradiated at a fixed location, and the same procedure is repeated at the next location separated by a spacing "*a*", to fabricate periodic surface structures on the entire surface area (Figure S1B; Videos S1, S2, and S3). For applications operating in the range of 1,000°C–2,000°C, the corresponding peak BB radiation wavelengths, λ_{max}, are respectively from 2.28 to 1.28 μm per Wien's displacement law. To choose the spacing, we considered the focused beam spot size of 30 μm, so the structural spacing remained below 35 μm to guarantee that the entire area was

Please cite this article in press as: Park et al., High-emissivity, thermally robust emitters for high power density thermophotovoltaics, Joule (2025), https://doi.org/10.1016/j.joule.2025.102005

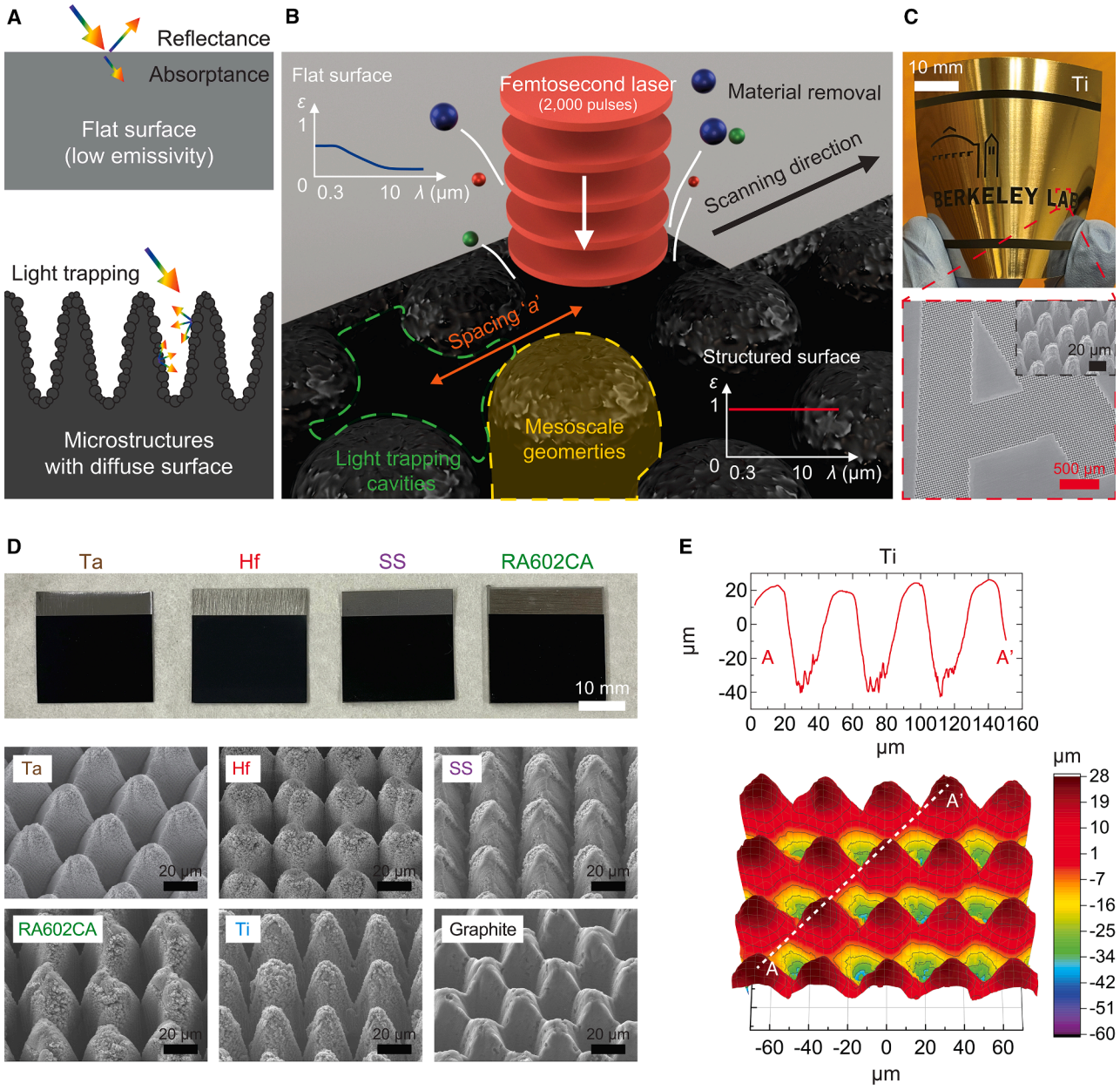

Figure 1. Fabrication of mesoscale structures via fs laser processing

(A) Light-material interaction with flat surfaces versus mesoscale geometries. Incident light is scattered and trapped by surface structures, producing additional light-material interactions that enhance total light absorption.

(B) Schematic depicting the fabrication of near-BB surfaces using ultrafast fs laser fabrication.

(C) Example of selective surface material texturing (dark regions) on a Ti foil (140-μm thickness). The SEM image shows the corresponding microstructure within the letter "A."

(D) Different substrates with mesoscale surface structures, characterized by digital (top) and SEM (bottom) images demonstrating scalability and versatility of the process. The black areas in the digital images represent the laser-processed area, while the gray areas represent the pristine substrate.

(E) Surface morphology of microstructures on Ti characterized by WLI. The white scale bar is 10 mm, the black scale bar is 20 μm, and the red scale bar is 500 μm.

processed by the laser. Further, to ensure the fabricated structures are sufficiently larger than λ_{max} to serve as efficient absorbers and emitters, the spacing "a" is chosen between 35 and 25 μm, depending on thermophysical properties of the materials. Note that spacings smaller than 25 μm can be achievable under the same experimental conditions, depending on the target application and associated temperature ranges.

Upon irradiation of sufficiently high fluence pulses, the metal surface experiences complex phase transitions whose coupled dynamics result in material removal in the forms of a plasma

Please cite this article in press as: Park et al., High-emissivity, thermally robust emitters for high power density thermophotovoltaics, Joule (2025), https://doi.org/10.1016/j.joule.2025.102005

plume, nanoparticles, and melt ejecta streaks.[34,54,55] Subsequently, remnant and redeposited melt matter is re-solidified into hierarchical microstructures featuring micro/nanoparticles, as characterized by scanning electron microscopy (SEM) images in Figures 1D and S2. Similar surface geometries can be obtained on different types of substrates using laser processing parameters in the same range as in the case of titanium (Ti). Due to the shallow absorption depth and the rapid energy deposition time of 500 fs, the extent of the heat affected zone into the irradiated material is limited. Furthermore, the temporal separation between successive pulses (i.e., 10 μs) is much longer than the timescale of surface melting and freezing and therefore prevents heat accumulation in the irradiated target. Similarly, the ablation plume dynamics also evolve at a faster timescale (~μs).[54] Consequently, the ablation process is in essence digital, eventually yielding microcavity recess depths in the range of 40 to 60 μm (aspect ratio ranges from 1.1 to 1.7), as measured by white light interferometry (WLI) in Figures 1E and S3. To achieve greater depths than 60 μm, increasing the laser fluence beyond the 2.1 J cm^{-2} and applying more than 2,000 laser pulses may be considered, depending on the material.

This ultrafast fs laser fabrication technique is more versatile than application of surface coatings, which are often bespoke to a specific material and face issues with high-temperature stability and adhesion.[24,56] The specific mesoscale surface geometries created with this technique are also difficult or impossible to create using other physical or chemical patterning methods such as reactive ion etching.[57] The fs laser processing technique is a simple, single-step, pigment and chemical-free method and is rapid and scalable.[50–52] Specifically, the processing speed for the benchtop system used in this work is 13.9 min cm^{-2}, but further improvements as presented in Note S2 and Figure S4A can accelerate processing 10-fold to ~1 min cm^{-2}. Likewise, at benchtop scales (~10 m^2) the processing cost is approximately \$2 cm^{-2}, but at an industrial scale of 100,000 m^2 the projected processing cost drops considerably to 0.04 ¢ cm^{-2} (Figure S4B).

Broadband augmented spectral emissivity enabled by LaBS

Figures 2A–2C, S5, and S6 show the hemispherical spectral emissivity and its standard deviation (SD) across the 0.3–15 μm wavelength range for both pristine surfaces and laser-textured microstructures of various materials, including metals (Ta, Ti, Al, hafnium [Hf], zinc [Zn], and niobium [Nb]), Ni/Ni-alloys (nickel [Ni], stainless steel, Inconel 600, and RA602CA), and carbon containing materials (graphite, carbon fiber composites [CFCs], tungsten carbide [WC], and molybdenum carbide [Mo_2C]). Pristine metal/metal alloys exhibit a spectral emissivity lower than 0.8 at short wavelengths that monotonically decreases as the wavelength increases. Pristine carbon materials exhibit a nearly flat, gray emissivity until the mid-IR, followed by a gradual decrease throughout the extended IR range. Nevertheless, near-BB emissivity is observed on all the laser-textured materials due to the development of the hierarchical surface morphologies shown in Figures 1D and S2. These surfaces have spectral emissivity higher than 0.96 with SDs below 0.0042 over the same wavelength range after fs laser processing, with an average emissivity exceeding 0.97 (Figure 2D). In addition, angle-resolved average emissivity measurements indicate that laser-fabricated microstructures can absorb incident light at up to a 75° angle (Figure 2E). Furthermore, we demonstrate that the spectral emissivity for a 200-μm thick Inconel LaBS is preserved even after folding at a 90° angle with a large radius of curvature (Figure S7). Given their optical behaviors closely resembling those of BBs,[15,17] we refer to them as LaBS.

To elucidate the origin of LaBS' optical properties, we conduct an analysis of their light-material interaction using finite-difference time-domain (FDTD) electromagnetic simulations using the software *Lumerical*. Wavy Ta microstructures (20-μm width and 40-μm height) with different surface roughnesses, mimicking laser-induced cavities decorated with micro/nanoparticles, are investigated (Figure 2F). For flat Ta with a smooth surface, both calculation and experimental measurement show a spectral reflectivity higher than 0.8 above 1-μm wavelength (Figure 2G). For wavy Ta structures with a smooth surface, absorption below 0.7-μm wavelength (visible spectrum) is prominent, while IR light is still strongly reflected due to higher impedance mismatching[28] with air at longer wavelengths (Figure S8). The introduction of surface roughness enhances light absorption, and the wavy Ta substrate with 2 μm roughness suffices to present a near-BB surface up to 10-μm wavelength (average emissivity of 0.95), which aligns well with experimental results (0.98 for a surface roughness of 2.22 ± 0.4 μm shown in Figure S9). Figure 2H and Video S4 show the electric field near the surface and clearly indicate that the incident light is trapped, scattered, and absorbed within microcavities due to the presence of surface roughness, compared with smooth wavy Ta structures. Moreover, the light-material interaction for flat Ta with different surface roughness is studied (Figure S10). Under the same surface roughness of 2 μm, light of longer than 7-μm wavelength is not fully absorbed (spectral reflectivity of 0.2 at 10-μm wavelength), further highlighting the significance of hierarchical microstructures in achieving near-BB surfaces.

Previous studies have indicated that the formation of oxide layers on surface geometries during fs laser processing can contribute to enhancing absorption in IR wavelengths, specifically for Al and steel substrates.[44,45] Our analysis using cross-sectional SEM and energy-dispersive X-ray spectroscopy confirms the presence of oxygen-containing layers of 2–4 μm thickness on Ti, Ta, and Hf microstructures (Figure S11). Oxide layers can contribute to increased absorption in certain IR ranges through phonon-polariton absorption[45,58,59] and help reduce refractive index mismatch. However, for our systems they are not the dominant cause of broadband near-BB emissivity. FDTD simulations show that the presence of oxide layers on microstructures have a measurable but smaller impact on the heightened light absorption compared with surface structuring effects (Figure S12). This is primarily attributed to the lower extinction coefficient of oxide materials in comparison to the high extinction coefficient of pure metals in the IR wavelength range[28] (0.24 for Ta_2O_5, and 54 for Ta at 10-μm wavelength). Therefore, combining the theoretical analysis in Figure 2G, we conclude that the major contributor to LaBS on different types of materials is the textured light-trapping cavities, consisting of micro/nanoparticles as well as microstructures.

Please cite this article in press as: Park et al., High-emissivity, thermally robust emitters for high power density thermophotovoltaics, Joule (2025), https://doi.org/10.1016/j.joule.2025.102005

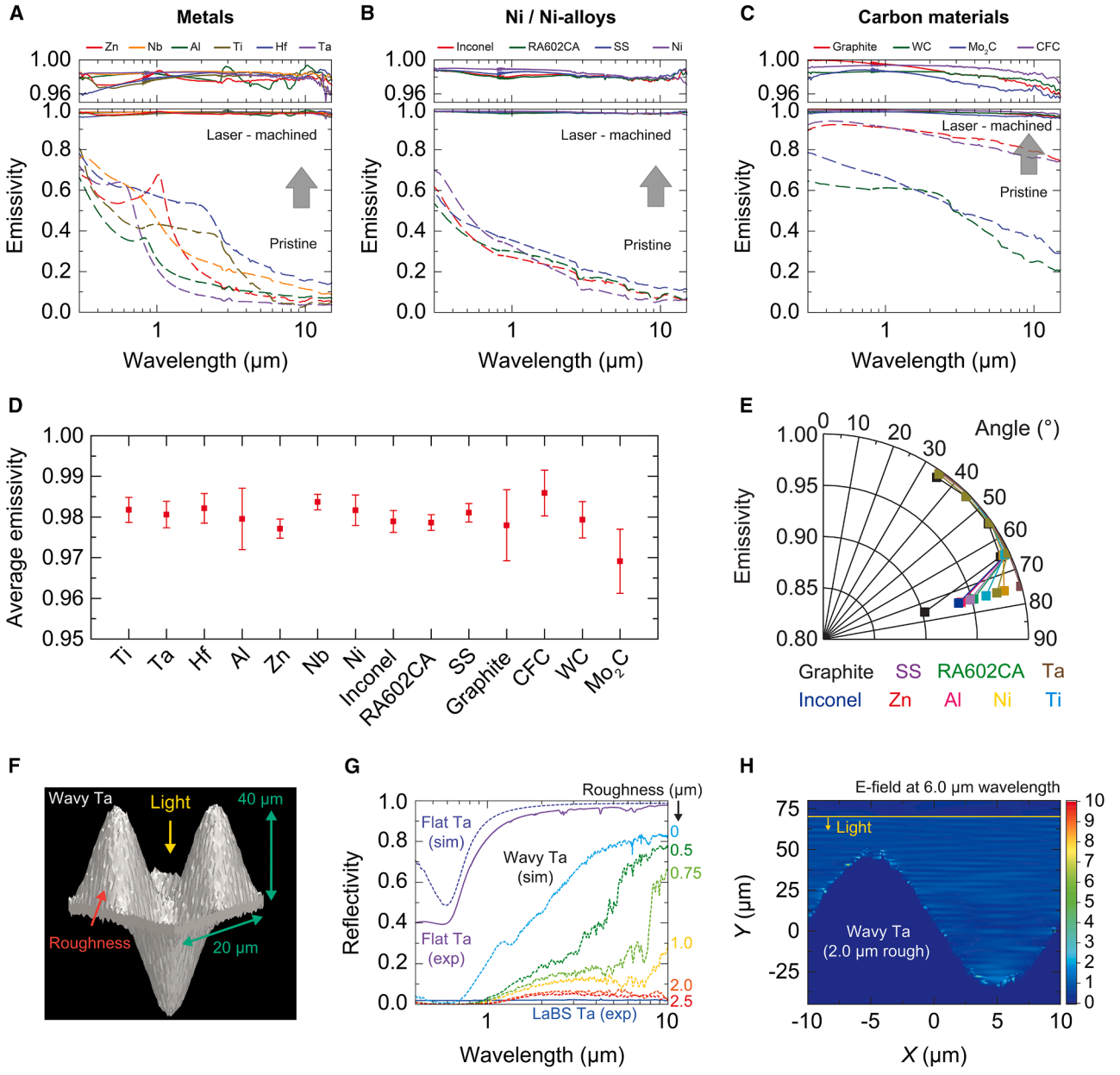

Figure 2. Optical properties of LaBS

(A–C) Hemispherical spectral emissivity of LaBS (solid lines) and pristine flat surfaces (dashed lines) for (A) metals (Zn, Nb, Al, Ti, Hf, and Ta), (B) Ni/Ni-alloys (Inconel, RA602CA, SS, and Ni), and (C) carbon materials (graphite, CFC, WC, and Mo_2C). Standard deviations across the 0.3- to 15-μm wavelength range are below 0.42% (0.0042 in emissivity), as shown in Figure S5.

(D) Spectrally integrated average emissivity of LaBS within 0.3 to 15-μm wavelength. Error bars represent the range of spectral emissivity across all wavelengths.

(E) Directional average emissivity of LaBS.

(F) Layout of wavy Ta topography with surface roughness, for input to FDTD simulations.

(G) Spectral reflectivity predicted by FDTD simulations (dotted lines; "sim") compared with experimental measurements (solid lines; "exp").

(H) Representative electric field at 6-μm wavelength for wavy Ta with 2-μm root-mean-squared surface roughness from FDTD simulations.

Enhancement in thermal emission and TPV electrical power density

TPVs are a promising emerging solid-state heat engine technology with broad applications including TES,[14,60] portable power generation,[61,62] and waste heat recovery.[63,64] Because TPVs' primary mechanism of energy transport and conversion is based on high-temperature thermal radiation, they are an ideal technology to benefit from LaBS. Our specific emphasis is on enhancing the electrical power density of a TPV cell, governed by both the emitter's spectral emissivity and temperature.

Please cite this article in press as: Park et al., High-emissivity, thermally robust emitters for high power density thermophotovoltaics, Joule (2025), https://doi.org/10.1016/j.joule.2025.102005

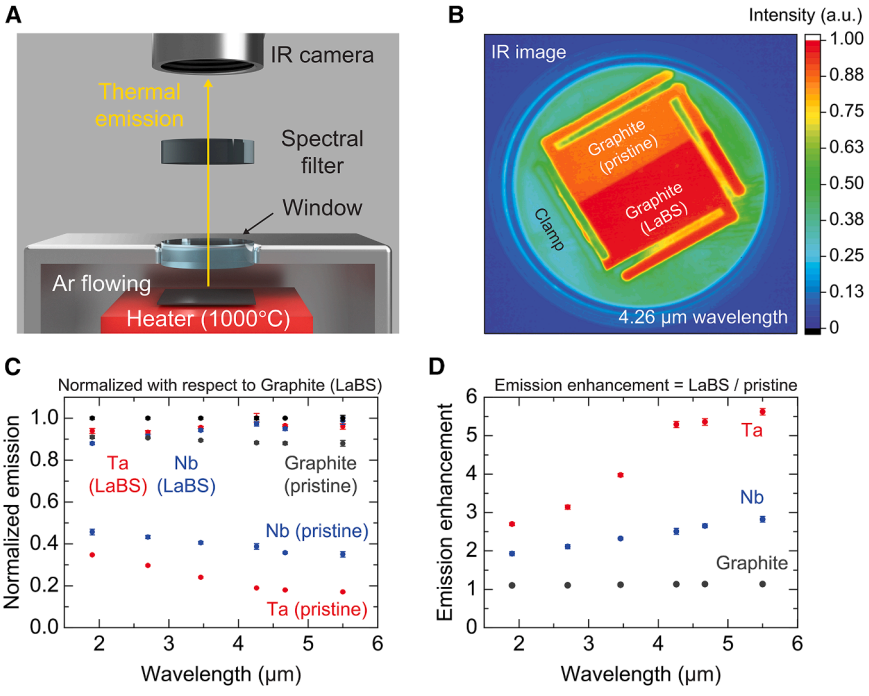

Figure 3. Augmentation of thermal emission in LaBS compared with pristine surfaces

(A) Schematic of thermal emission measurement using an IR camera and spectrally selective filters. The target samples are heated to 1,000°C inside an Ar flowing chamber using a resistive heater. Thermal emission is quantified using a photon counting method.

(B) An example of acquired IR images for graphite at 4.26-μm wavelength.

(C) Thermal emission for Ta and Nb LaBS, as well as pristine Ta, Nb, and graphite, normalized with respect to graphite LaBS. Error bars indicate 1 SD uncertainties in thermal emission measurements.

(D) Emissive power enhancement between LaBS and pristine surfaces.

It is important to first verify that an enhancement in room temperature spectral emissivity can result in increased thermal emission at elevated temperatures. We therefore quantify thermal emission enhancement for LaBS as compared with pristine surfaces at a temperature of 1,000°C (Figure 3A). A set of IR camera and spectral filters is used to measure the thermal emission intensity using a photon counting method at specific wavelengths (refer to details in Figure S13). Figures 3B and 3C show the thermal emission normalized to graphite LaBS. Emission for Ta and Nb LaBS surpasses that of pristine graphite (gray points) across most of the measured spectral range and closely approaches graphite LaBS (black points) within the wavelength range of 1.9–5.5 μm. In contrast, pristine Ta and Nb surfaces emit less than half this amount. This observation indicates that laser-textured metallic substrates can emit spectrally flat, "gray" thermal radiation like the well-known behavior of graphite in the IR wavelength range. This characteristic is not usually accessible for pristine metal surfaces, as discussed in Figure 1. The calculated emission enhancement factors (ratios between LaBS and pristine surfaces) shown in Figure 3D quantify thermal emission increases of 170% to 460% for Ta, 100% to 170% for Nb, and 10% for graphite, depending on the considered wavelength.

We experimentally demonstrate that the increase in thermal emission due to LaBS enhances the generated electrical power density in two tandem TPV cells with band gaps of 1.4/1.2 eV (Figure 4) and 1.2/1.0 eV (Figure S14). We place thermal emitters directly above the TPV cells (Figures 4A and 4B) and measure the electrical power density and heat absorbed as a function of emitter temperature. We test different thermal emitters including CFC, Ta LaBS (Figure S15; Video S5), and plain Ta in the temperature range of 1,700°C (peak energy of 0.84 eV) to 2,200°C (peak energy of 1.06 eV), selected to mimic TPV application-relevant temperatures. As indicated by the external quantum efficiency and reflectance curves in Figure 4C, photons emitted above the lower band gap (either 1.2 or 1.0 eV) can be absorbed by the TPV cell and converted to electricity, while unusable photons emitted below the band gap are back-reflected and recycled at the emitter. Accordingly, the greater the number of photons emitted above the band gap, the higher the electrical current produced by the same TPV.

Figures 4D–4F and S14C–S14E show generated electrical current density versus voltage (IV) measurements of the TPV cells with a cell area of 0.7145 cm^2, using different emitters set at various temperatures. For the 1.4/1.2 eV TPV cell, the short circuit current density using the CFC emitter is 2.11 A cm^{-2}, Ta LaBS is 2.04 A cm^{-2}, and plain Ta is 1.22 A cm^{-2} at 2,200°C. Moreover, the power density calculated by dividing the electrical power at the maximum power point by the TPV cell area is shown in Figure 4G, and power density versus voltage (PV) plots are presented in Figures S16 and S17. At 2,200°C, the power density using the CFC emitter is 4.14 W cm^{-2}, Ta LaBS is 4.10 W cm^{-2}, and plain Ta is 2.19 W cm^{-2}. Similar enhancements are observed when using the 1.2/1.0 eV TPV cell (Figure S14F). The Ta LaBS emitter increases the TPV power density nearly 2-fold, approaching that of the CFC emitter—but using a material with 3 orders of magnitude lower vapor pressure,[18] enhancing TPV lifetime due to lower rates of deposition on the cell.[19,67]

Note that in practice the TPV efficiencies and power densities at low temperatures (<1,800°C) could be significantly further improved by using lower band-gap cells designed for those temperatures (as demonstrated in Roy-Layinde et al.[68] and Tervo et al.[66]). Similar relative improvements in power density from using LaBS emitters would then be expected for those devices. This increase in power density is critical for the technoeconomics of TPV systems as it reduces the total cell area required,[1,14] potentially halving the cost of electricity produced in certain cost scenarios (e.g., from 30 to 18 ¢/kWh in a system where TPV costs dominate[13,69]). LaBS therefore have the potential to nearly double the profitability of TPV technologies in ideal conditions. In summary, the emissivity measurements (Figure 2) and

Please cite this article in press as: Park et al., High-emissivity, thermally robust emitters for high power density thermophotovoltaics, Joule (2025), https://doi.org/10.1016/j.joule.2025.102005

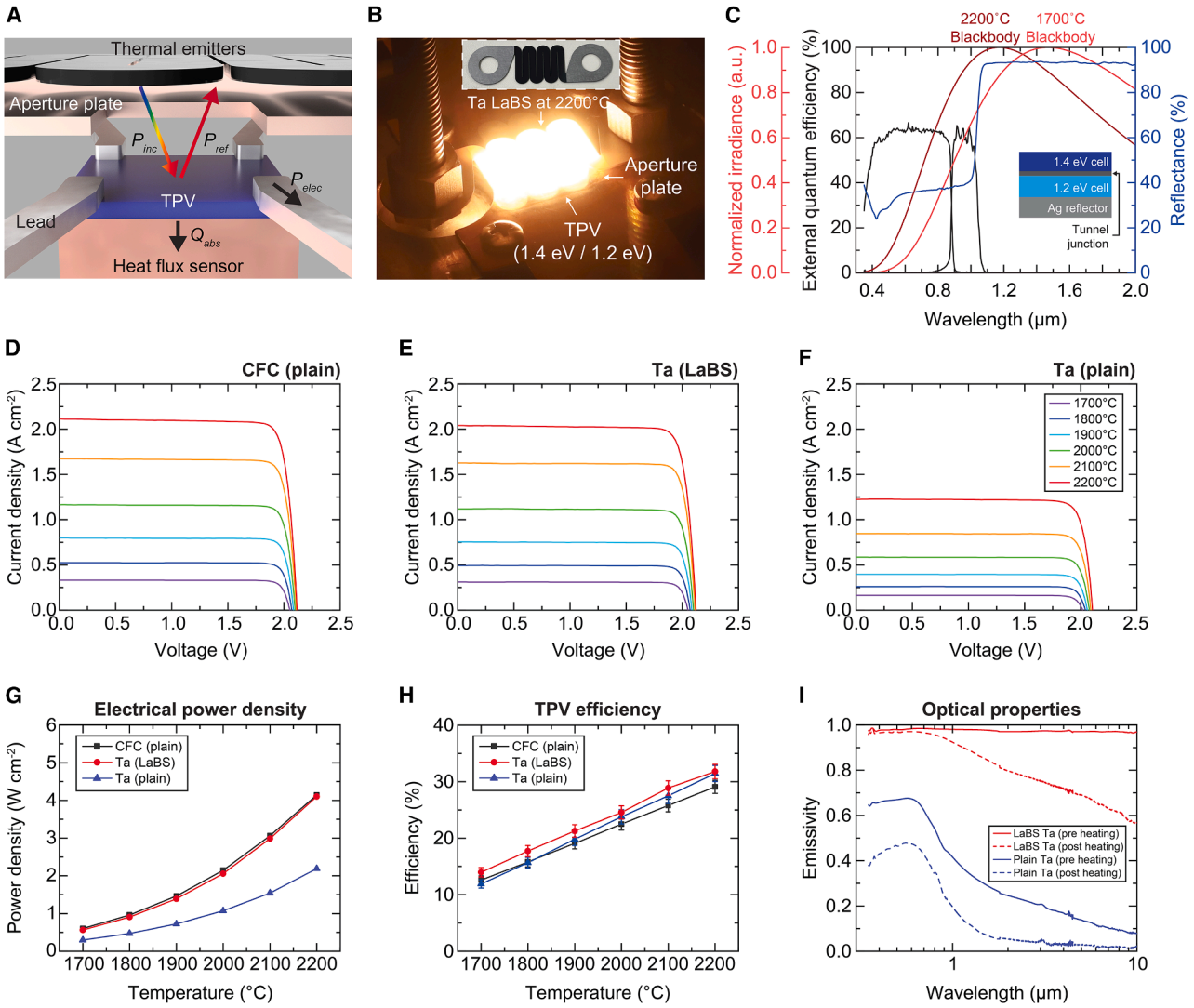

Figure 4. Characterization of a tandem TPV cell with 1.4/1.2 eV band gaps using different thermal emitters

(A) Schematic of TPV characterization[65,66] with Ta LaBS.

(B) Picture of the TPV characterization system with the Ta LaBS at 2,200°C functioning as the TPV thermal emitter (inset: Ta LaBS at room temperature).

(C–F) External quantum efficiency and reflectance of the 1.4/1.2 eV tandem TPV cell, with normalized BB emission spectra at 2,200°C and 1,700°C overlaid. The inset illustrates a simplified schematic of the TPV cell structure with the full schematic available in LaPotin et al.[1] Current density-voltage (IV) curves for TPV cells powered by (D) CFC, (E) Ta LaBS, and (F) plain Ta, respectively, for emitter temperatures ranging from 1,700°C to 2,200°C.

(G) Generated electrical power density at maximum power point of the TPV cell as a function of emitter temperature.

(H) TPV heat-to-electricity energy conversion efficiency measurements, error bars indicate 1 SD uncertainties in heat flux measurements.

(I) Optical property measurements for Ta LaBS and plain Ta before and after heating.

spectral thermal emission measurements (Figure 3) confirm that LaBS achieve a significant improvement in broadband thermal emission, leading to higher photon emission flux above 1.2 eV and therefore an increased TPV power density.

Increasing TPV power density is only helpful if doing so does not simultaneously reduce its heat-to-electricity conversion efficiency. TPV efficiency, η, can be calculated by comparing the electrical power generated to the heat absorbed:

$$\eta = \frac{P_{elec}}{P_{elec}+Q_{abs}} \quad \text{(Equation 1)}$$

where P_{elec} is the electrical power and Q_{abs} is the heat absorbed by the TPV cell, both at the maximum power point. Q_{abs} is measured simultaneously with power using a custom-built heat flux sensor. Detailed experimental calibrations are presented in the methods section and Figures S18 and S19. As shown in Figures 4H and S14G, the TPV efficiency using the CFC emitter was 29.07% ± 1.16%, Ta LaBS was 31.79% ± 1.27%, and plain Ta was 31.45% ± 1.44% at 2,200°C. There is thus no statistically significant difference in the TPV efficiency between using the Ta LaBS versus the plain Ta emitter, both of which yield comparable

Please cite this article in press as: Park et al., High-emissivity, thermally robust emitters for high power density thermophotovoltaics, Joule (2025), https://doi.org/10.1016/j.joule.2025.102005

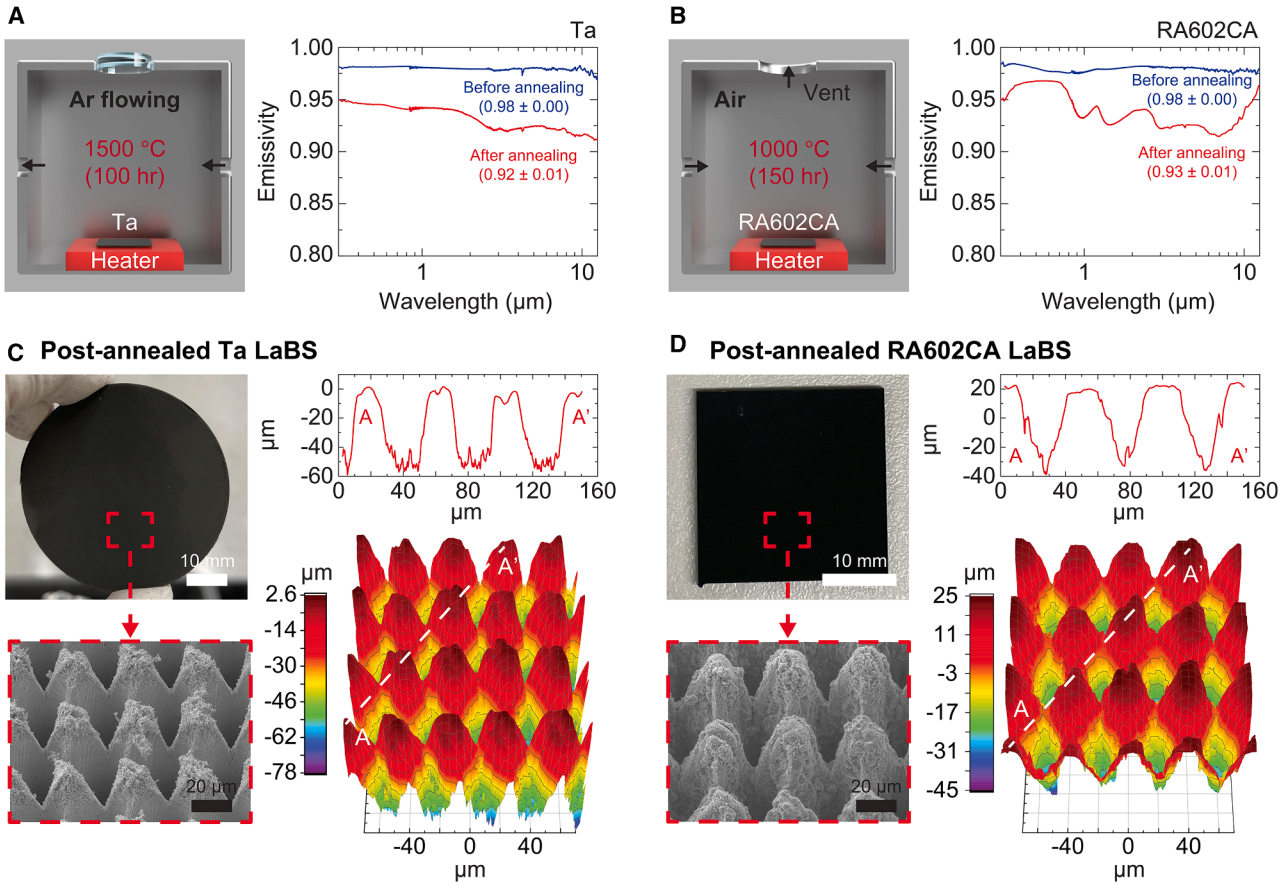

Figure 5. Thermal stability characterization of Ta and RA602CA LaBS

(A) Spectral emissivity before and after annealing Ta LaBS at 1,500°C for 100 h in Ar.

(B–D) Spectral emissivity before and after annealing RA602CA LaBS at 1,000°C for 150 h in ambient air. Error bars represent the range of spectral emissivity across all wavelengths. Surface morphologies characterized by SEM and WLI for post-annealed (C) Ta and (D) RA602CA LaBS. White scale bars are 10 mm, and black scale bars are 20 μm.

TPV efficiencies to using a CFC emitter. This result points to the importance of the TPV cell's gold (Au) back-reflector mirror, which significantly reduces parasitic heating from sub-band-gap photons even for the broadband high-emissivity Ta LaBS and CFC emitters. We note that high TPV cell efficiency does not necessarily translate to high system efficiency if this reflected light is unable to make it back to the emitter, such as for open-cavity systems. Therefore, spectrally selective emitters may be necessary for designs lacking good sub-band-gap photon recycling, and related studies have investigated how to use the laser ablation technique presented in this work to design selective emitters.[51]

We can use these tests as an indication of high-temperature stability. During the experiments we held each temperature for 10 min, and used another 5 min to tune the power supply to reach the next temperature, for a total of 90 min of high-temperature stability testing from 1,700°C to 2,200°C. We find that compared with the plain Ta emitter, the Ta LaBS exhibits significantly reduced in-band performance degradation after a cumulative 90 min of heating at these temperatures, as shown in Figures 4I and S20. The Ta LaBS in-band (above band gap) emissivity decreases from 0.982 to 0.947, while the out-of-band (sub band gap) emissivity decreases from 0.974 to 0.807 (spectrally weighted at 2,200°C).

Thermal stability of LaBS

Finally, we perform targeted experiments and theoretical modeling to investigate the mechanisms of thermal degradation in LaBS in refractory materials. Thermal stability is critical for practical applications to reduce the number of replacements necessary over a system's lifetime. Thermal stability testing of Ta LaBS (Video S6) and RA602CA LaBS are shown in Figure 5. These materials are selected because refractory metals are commonly used in TPV systems due to their high melting point above 2,500°C, while oxidation-resistant Ni superalloys are often employed in applications where the system operates in ambient air (e.g., CSP).[70]

We subject the Ta LaBS to heating at 1,500°C for 100 h in an Ar flowing chamber (Figures 5A and S21) while the RA602CA LaBS is annealed at 1,000°C for 150 h under ambient air (Figure 5B).

Please cite this article in press as: Park et al., High-emissivity, thermally robust emitters for high power density thermophotovoltaics, Joule (2025), https://doi.org/10.1016/j.joule.2025.102005

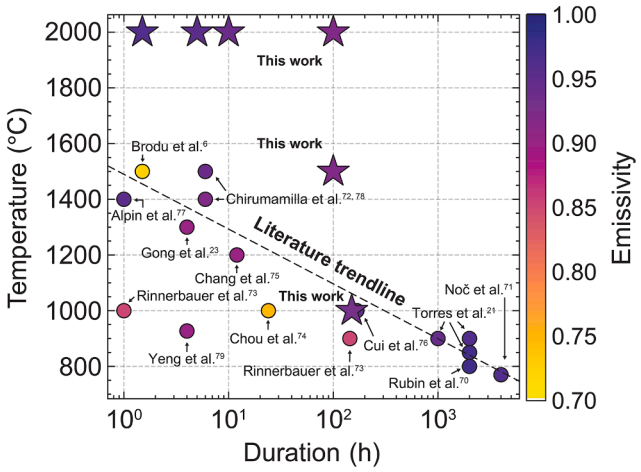

Figure 6. Comparison with high-temperature stability from literature

Results from stability tests of current state-of-the-art thermal emitters in the literature (circles)[21,22,24,71–79] plotted alongside this work (stars). Each point shows the duration of time that an emitter was held at a specific temperature, and the fill color shows its emissivity at 1 μm measured after the test as indicated by the color bar. Emissivity at 1 μm is chosen for consistent comparison among the various emitters that included both spectrally selective and broadband emitters. The trendline, fitted only to the state-of-the-art literature data, is a line on these log-linear axes because degradation rates increase exponentially with temperature.

After annealing, the Ta LaBS has an average emissivity of 0.92 (between 0.3- and 15-μm wavelengths), while RA602CA LaBS has an average emissivity of 0.93, constituting an average emissivity drop of 0.06 or less for both LaBS. SEM images and WLI measurements, as presented in Figures 5C and 5D, indicate that mesoscale geometries are preserved without clear evidence of thermal damage or deformation on the microstructures. Additionally, the directional spectral absorptivity at different angles up to 1.1-μm wavelength remains above 0.96 after annealing (Figure S22), implying that the ability for the near-omnidirectional light absorption is maintained.

Next, we conducted higher-temperature stability tests using the Ta LaBS serpentine emitters from the previous section, as detailed in Figure S23. We subject the Ta LaBS emitters to heating at 2,000°C for 100 h, in an inert Ar atmosphere with 10^{-19} atm O_2 partial pressure. Emissivity measurements were taken at 1.5, 5, 10, and 100 h, as presented in Figure S23B. The in-band emissivity drops to 0.96 after 1.5 h, 0.95 after 5 h, 0.94 after 10 h, and 0.92 after 100 h. To further demonstrate practicality, we have conducted thermal cycling tests between room temperature and 2,000°C, holding at each for 2 min with a ramp time of 30 s. As shown in Figure S24, the emissivity of the emitter remains high after 10 cycles, with in-band emissivity > 0.94.

We have plotted our stability results alongside other relevant results from the literature in Figure 6. As seen by the literature data-fitted trendline, most durability studies are done either at high temperature (>1,200°C) for short durations (<10 h), or low temperature (<900°C) for long durations (>1,000 h). There is a noticeable gap of emitters (either selective or broadband) that have been characterized for both long durations and high temperatures. Our 100-h tests at 1,500°C and 2,000°C meet this gap and are the highest-temperature durability tests of a structured emitter, to our knowledge.

We believe the micro/nanostructures formed by fs laser processing can be robust and durable because they are generated from the substrate itself. In other words, their bulk characteristics (e.g., melting point and oxidation resistance) should be maintained after laser processing, resulting in high thermal stability along with stable long-term radiative properties, if using high-temperature materials. However, we have observed that the micro/nanoparticles attached on Ta microstructures undergo sintering during prolonged heating at elevated temperatures. This sintering causes surface smoothening and decreased particle packing density, as evident from SEM images (Figure S25), leading to a reduction in spectral absorptivity, as illustrated in Figure 2G. As a result, we anticipate that the optical properties of flat Ta with surface roughness will eventually revert to those of the original flat Ta without surface roughness (i.e., low emissivity, as shown in Figure S10B). However, wavy surface structuring provides a second layer of optical property control with larger length scale features that are slower to degrade. Even for locally smooth surfaces lacking surface roughness, high spectral emissivity near a 1-μm wavelength is still preserved for Ta that has these larger length scale wavy microstructures (Figure 2G). Therefore, introducing these wavy microstructures, in addition to the surface roughness provided by the micro/nanoparticles, helps extend the emitter's useful operational lifetime.

To quantify this sintering process, we developed a model to predict how the emissivity would change for long durations or high temperatures (Note S3). In a slightly oxidizing atmosphere of 10^{-6} atm pO_2 (Figures S26A–S26C), we predict that the Ta LaBS could retain its high broadband emissivity (>0.96) for up to 100,000 h at temperatures below 1,300°C. At temperatures above 1,500°C, shorter lifetimes are anticipated due to surface smoothening caused by the high vapor pressure of Ta_2O_5 and its melting point of 1,872°C. In contrast, under a reducing atmosphere (10^{-19} atm pO_2 as in the TPV measurements, Figures S26D–S26F), the initial average emissivity is expected to be lower because of the early removal of rough Ta_2O_5 nanoparticles. Nevertheless, the lifetime at high temperatures is projected to be longer, lasting 10,000 h at 2,000°C, due to the lower vapor pressure and higher melting point of Ta compared to Ta_2O_5. The impact of improving durability on cost is presented in Figure S4C.

All in all, these results are promising for applications in TPV and CSP, where traditional surface coatings often fail due to detrimental delamination.[70] By engineering the light-absorbing media directly on bulk substrates, we can avoid coating adhesion and delamination issues and achieve near-black emissivity at high temperatures for long lifetimes.

Conclusions

We demonstrate LaBS with a spectral emissivity exceeding 0.96 across a wide wavelength range across different substrates using ultrafast fs laser ablation, well-suited for enhancing thermal radiative energy transport in energy applications. By decoupling surface optical properties from bulk characteristics, LaBS exhibit thermal stability and enhanced thermal emission, maintaining superior spectral absorptivity after exposure to elevated temperatures exceeding 1,000°C for extended

Please cite this article in press as: Park et al., High-emissivity, thermally robust emitters for high power density thermophotovoltaics, Joule (2025), https://doi.org/10.1016/j.joule.2025.102005

periods including in air. Furthermore, TPV power density can more than double when using a LaBS compared with a plain emitter without any loss in efficiency. While the current study focuses on TPV and CSP applications, our scalable approach utilizing ultrafast laser-matter interactions can be easily generalized to various energy harvesting and thermal management applications, including solar water desalination, passive radiative cooling, and spacecraft, where enhancing radiative energy transport is of particular importance for achieving better performance and efficiency.

METHODS

Materials

Al, Inconel 600, Ti, stainless steel 301, Ni, graphite, Hf, and Zn substrates were purchased from GoodfellowUSA. Ta substrates were obtained from Sigma Aldrich and GoodfellowUSA and ship with a native oxide layer as confirmed in Figure S27. RA602CA substrates were purchased from Rolled Alloys. Nb substrates were purchased from Thermo Scientific. WC and Mo_2C substrates were available from Stanford Advanced Materials. Detailed specifications of materials are summarized in Table S1. As-received materials were used for laser processing without further surface polishing.

Ultrafast fs laser processing

A 500-fs laser with 1,030-nm wavelength operating at 100 kHz repetition rates (s-Pulse, Amplitude) was synchronized with a galvano scanner (excelliSCAN 14, SCANLAB), and *XYZ* stages (A-311 *XY* air-bearing stages with L-310 vertical stage, PI-USA). The focused beam spot size was 30 μm. The processing rate to fabricate LaBS, as shown in Figures 1B and S1B, is approximately 0.072 cm^2 per min. After fs laser processing, the fabricated samples were sonicated in deionized water for 1 h to remove weakly adsorbed particles on the surface.

Optical property characterization

For visible wavelength ranges (<0.8-μm wavelength), a UV-vis spectrophotometer (Lambda 950, Perkin-Elmer) with a 150-mm integrating sphere was used to measure the hemispherical spectral reflectivity. For IR spectral ranges (>0.8-μm wavelength), a Fourier transform IR spectrometer (Nicolet iS50, ThermoFisher Scientific) equipped with an integrating sphere (Pike technologies) was used. Because none of the substrates are transparent in the IR regime, the spectral absorptivity/emissivity was calculated by "1 − reflectivity." Detailed optical property measurement procedures are provided in Figure S6. An accessory component (VeeMax III, Pike technologies) was used to measure the directional specular emissivity.

Surface morphology characterization

SEM (JEOL), WLI (NewView 6000, Zygo), and laser confocal microscopy (VK-X3000, Keyence) were used to examine the surface morphology.

FDTD simulation

FDTD simulations were performed using *Lumerical* software. The simulated structure, shown in Figure 2F, features domain sizes of 20 μm in both the *X* and *Y* directions, with an amplitude of 40 μm and a thickness of 5 μm. The mesh size is set to 50 nm in the *X* and *Y* directions and 100 nm in the *Z* direction. Periodic boundary conditions are applied in the *XY* plane, while perfectly-matched-layer boundary conditions are used in the *Z* direction. Different surface roughnesses are generated using the built-in script (ID: rough_surf), maintaining a consistent correlation length of 0.1 μm, but varying the root-mean-squared amplitudes. The auto-off value is set to 1×10^{-6}. The simulated spectral emissivity is derived from the simulated spectral reflectivity (i.e., emissivity = 1 − reflectivity). We conducted the FDTD simulations using a workstation equipped with an Intel Xeon CPU E5-2687W v.3 (3.10 GHz) and 64 GB of random access memory (RAM). Under these conditions, each simulation was completed in approximately 12 h.

Thermal emission measurement

Thermal emission was measured by an IR camera (Spark M150, Telops) and spectral bandpass filters (Iridian Spectral Technologies) with central wavelengths at 1.9, 2.7, 3.46, 4.26, and 4.46 μm. Samples were heated by a heater (Model #101491, HeatWave Labs) in an Ar gas flowing chamber (Praxair, 99.999% ultrahigh purity), and the temperature was measured by an embedded K-type thermocouple.

TPV measurement

The TPV cells used are a 1.4/1.2 eV tandem GaAs/GaInAs cell with a silver (Ag) back-surface reflector (MT618, National Renewable Energy Laboratory) and a 1.2/1.0 eV tandem AlGaInAs/GaInAs cell with a Au back-surface reflector (MT671, National Renewable Energy Laboratory). Detailed schematics of the TPV cell structures are presented in LaPotin et al.[1] We use III–V tandem cells with a back reflector to improve performance by reducing thermalization and parasitic heat absorption. TPV power is measured by a 4-wire measurement (Keithley) using electrical leads placed on the top and bottom contacts of the cell. At each temperature, an IV curve is obtained using the 4-wire measurement and the maximum power point is determined. At that maximum power point, the electricity produced and heat absorbed are measured and efficiency is calculated.

Heat absorbed is measured with a custom-built heat flux sensor that is calibrated according to prior methodology.[65] The custom heat flux sensor consists of a copper bar with 4 thermocouples embedded in it. The bottom of the copper bar is kept at 5°C using a thermoelectric, and the TPV cell is attached to the top with thermal paste.

From the electrical power output and heat absorption values, the efficiency can be calculated (using Equation 1), but there are sources of superfluous heating from the measurement apparatus that must be accounted for. Although the electrical lead placement is designed to minimize superfluous heating by conduction to the emitter, some heat absorption by the measurement leads is inevitable, which would cause an underestimate of efficiency.[80] To correct for this superfluous absorption, at each considered temperature the heat absorbed is measured with ($Q_{voc,leads}$) and without ($Q_{Voc,no\ leads}$) the electrical leads in place, both at open circuit conditions. The difference in heat absorbed is thus the contribution of superfluous heating of the

leads and is plotted in Figure S18. Another source of superfluous heating is Joule heating at the contact of the electrical lead to the cell,[80] so the contact resistance ($R_{contact}$) was measured to be 0.092 ohms and the extra heating was accounted for with $I^2R_{contact}$, where I is the current generated by the TPV cell at its maximum power point. Therefore, the calibrated heat absorption is calculated by subtracting these superfluous sources of heat from the total heat measured by the heat flux sensor (Q_{HFS}):

$$Q_{abs} = Q_{HFS} - \left(Q_{Voc,leads} - Q_{Voc,no\ leads}\right) - I^2R_{contact} \quad \text{(Equation 2)}$$

After conducting this calibration and calculating the efficiency, we note that the values are significantly less than those reported in LaPotin who reported a 37% efficiency using the same experimental setup with a CFC emitter.[65] Therefore, it is likely the cells used in this work are lower quality with worse quantum efficiency and higher series resistance than the best quality cells of the same architecture. Future experiments could use higher quality cells and achieve better efficiency.

The measurement was conducted in a chamber with oxygen partial pressure controlled to 10^{-18} atm to limit the oxidation of the Ta sample. To achieve these low oxygen partial pressures, a crucible of zirconium powder (Strem) was heated to >600°C inside the chamber, reacting with the oxygen to form zirconia.

The emitter was heated with Joule heating by supplying a current with a power supply (MagnaDC). To match the electrical resistance properties of the emitter with the specifications of the power supply, the CFC emitters were made as a monolithic piece while the Ta emitters had a serpentine pattern, as shown in Figure S15 and Video S5. However, the monolithic piece had the same view factor as the serpentine path, as verified in both simulation and experiment (Figure S19). The emitters were placed 5 mm above the TPV cell to achieve a high view factor of 0.39, with an aperture plate placed in between to limit parasitic heat absorption in components around the cell.

This view factor most closely corresponds to a system configuration where the emitter area is smaller than the cell area (e.g., concentric cylinders with cells on the outer cylinder). These configurations are typically characterized by low power density, but we have shown the LaBS emitters can help offset this limitation and achieve higher power density due to their higher emissivity. Other studies have examined higher view factors in configurations where the emitter and cells are closer together or where the emitter fully surrounds the cells. These studies found that while higher view factors tend to reduce efficiency (due to increased series losses), they increase power density by increasing the current density.[81] We note that increasing emitter emissivity would enhance power density for any view factor configuration, if holding all other parameters constant.

The temperature of the emitter was measured using a two-color pyrometer (Fluke Endurance E1RH) placed above the emitter. The top surface of the Ta emitters was LaBS to ensure constant emissivity in the two measurement bands (centered at 0.95- and 1.05-μm wavelengths). The emitter was held at each temperature for 10 min to ensure a thermal steady state was reached. IV curves were taken after 5 min at each temperature, and the power and heat absorption values were averaged over the last 5 min of each temperature.

Thermal stability test

A box furnace (Lindberg/Blue M 1,100°C, Thermo Fisher Scientific) was used to anneal RA602CA substrates in ambient air. A custom sublimation chamber built by Antora Energy was used to anneal Ta substrates at 1,500°C under Ar gas condition.

Further details regarding the methods can be found in the supplemental information.

RESOURCE AVAILABILITY

Lead contact

Requests for further information and resources should be directed to and will be fulfilled by the lead contact, Vassilia Zorba (vzorba@lbl.gov).

Materials availability

The LaBS samples generated in this study are stored at Lawrence Berkeley National Laboratory, while the TPV cells are stored at the Massachusetts Institute of Technology and the National Renewable Energy Laboratory. These can be made available upon request for collaboration, but we may require a payment and/or a completed materials transfer agreement if there is potential for commercial application.

Data and code availability

The authors declare that the data supporting the findings of this study are included within the article and its supplemental information and will be available by the lead contact upon request.

ACKNOWLEDGMENTS

The authors thank Antora Energy Inc. for the use of one of their sublimation chambers. The authors thank Myles Steiner and the Chemistry and Nanoscience Center at the National Renewable Energy Laboratory for providing the TPV cells used in the study. The authors thank Duo Xu and the Boriskina Research Lab/NanoEngineering Group for lending the integrating sphere used for part of the reflectance measurements in this work. This work was carried out in part through the use of MIT.nano's Characterization facilities.

This work was supported by the Laboratory Directed Research and Development program of Lawrence Berkeley National Laboratory under US Department of Energy contract no. DE-AC02-05CH11231 and the ARPA-E contract no. 2107-1539 to Lawrence Berkeley National Laboratory. This work was partially supported by Solar Energy Technologies Office under US Department of Energy contract no. DE-EE0009819. This work was supported by the National Science Foundation Graduate Research Fellowship under award no. 2141064.

AUTHOR CONTRIBUTIONS

Conceptualization, M.P., S.V., A.L., R.P., A.H., S.D.L., C.P.G., and V.Z.; methodology, M.P., S.V., A.L., D.P.N., R.P., A.H., S.D.L., C.P.G., and V.Z.; investigation, M.P., S.V., and A.L.; supervision, R.P., A.H., S.D.L., C.P.G., and V.Z.; writing—original draft, M.P., S.V., A.L., R.P., A.H., S.D.L., C.P.G., and V.Z.; writing—review and editing, M.P., S.V., A.L., R.P., A.H., S.D.L., C.P.G., and V.Z.

DECLARATION OF INTERESTS

The authors declare no competing interests.

SUPPLEMENTAL INFORMATION

Supplemental information can be found online at https://doi.org/10.1016/j.joule.2025.102005.

Received: December 24, 2024
Revised: March 25, 2025
Accepted: June 5, 2025

REFERENCES

1. LaPotin, A., Schulte, K.L., Steiner, M.A., Buznitsky, K., Kelsall, C.C., Friedman, D.J., Tervo, E.J., France, R.M., Young, M.R., Rohskopf, A., et al. (2022). Thermophotovoltaic efficiency of 40%. Nature *604*, 287–291. https://doi.org/10.1038/s41586-022-04473-y.
2. Fan, D., Burger, T., McSherry, S., Lee, B., Lenert, A., and Forrest, S.R. (2020). Near-perfect photon utilization in an air-bridge thermophotovoltaic cell. Nature *586*, 237–241. https://doi.org/10.1038/s41586-020-2717-7.
3. Lenert, A., Bierman, D.M., Nam, Y., Chan, W.R., Celanović, I., Soljačić, M., and Wang, E.N. (2014). A nanophotonic solar thermophotovoltaic device. Nat. Nanotechnol. *9*, 126–130. https://doi.org/10.1038/nnano.2013.286.
4. Weinstein, L.A., Loomis, J., Bhatia, B., Bierman, D.M., Wang, E.N., and Chen, G. (2015). Concentrating Solar Power. Chem. Rev. *115*, 12797–12838. https://doi.org/10.1021/acs.chemrev.5b00397.
5. He, Y.-L., Qiu, Y., Wang, K., Yuan, F., Wang, W.-Q., Li, M.-J., and Guo, J.-Q. (2020). Perspective of concentrating solar power. Energy *198*, 117373. https://doi.org/10.1016/j.energy.2020.117373.
6. Brodu, E., Balat-Pichelin, M., Sans, J.L., Freeman, M.D., and Kasper, J.C. (2015). Efficiency and behavior of textured high emissivity metallic coatings at high temperature. Mater. Des. *83*, 85–94. https://doi.org/10.1016/j.matdes.2015.05.073.
7. He, X., Li, Y., Wang, L., Sun, Y., and Zhang, S. (2009). High emissivity coatings for high temperature application: Progress and prospect. Thin Solid Films *517*, 5120–5129. https://doi.org/10.1016/j.tsf.2009.03.175.
8. Singh, S.C., ElKabbash, M., Li, Z., Li, X., Regmi, B., Madsen, M., Jalil, S.A., Zhan, Z., Zhang, J., and Guo, C. (2020). Solar-trackable super-wicking black metal panel for photothermal water sanitation. Nat. Sustain. *3*, 938–946. https://doi.org/10.1038/s41893-020-0566-x.
9. Menon, A.K., Haechler, I., Kaur, S., Lubner, S., and Prasher, R.S. (2020). Enhanced solar evaporation using a photo-thermal umbrella for wastewater management. Nat. Sustain. *3*, 144–151. https://doi.org/10.1038/s41893-019-0445-5.
10. Ni, G., Li, G., Boriskina, S.V., Li, H., Yang, W., Zhang, T., and Chen, G. (2016). Steam generation under one sun enabled by a floating structure with thermal concentration. Nat. Energy *1*, 16126. https://doi.org/10.1038/nenergy.2016.126.
11. Chen, J., Lu, L., Gong, Q., Lau, W.Y., and Cheung, K.H. (2021). Techno-economic and environmental performance assessment of radiative sky cooling-based super-cool roof applications in China. Energy Convers. Manag. *245*, 114621. https://doi.org/10.1016/j.enconman.2021.114621.
12. Rafique, M., and Bahaidarah, H.M.S. (2021). Impacts of solar intensity on the techno-economic feasibility of high temperature particle receiver technology. J. Cleaner Prod. *285*, 124908. https://doi.org/10.1016/j.jclepro.2020.124908.
13. Verma, S., Buznitsky, K., and Henry, A. (2025). Thermophotovoltaic performance metrics and techno-economics: Efficiency vs. power density. Appl. Energy *384*, 125479. https://doi.org/10.1016/j.apenergy.2025.125479.
14. Amy, C., Seyf, H.R., Steiner, M.A., Friedman, D.J., and Henry, A. (2019). Thermal energy grid storage using multi-junction photovoltaics. Energy Environ. Sci. *12*, 334–343. https://doi.org/10.1039/C8EE02341G.
15. Brewster, M.Q. (1992). Thermal Radiative Transfer and Properties (Wiley).
16. Grigoropoulos, C.P. (2009). Transport in Laser Microfabrication: Fundamentals and Applications (Cambridge University Press). https://doi.org/10.1017/CBO9780511596674.
17. Howell, J.R., Mengüç, M.P., Daun, K., and Siegel, R. (2020). Thermal Radiation Heat Transfer, Seventh Edition (CRC Press). https://doi.org/10.1201/9780429327308.
18. Lide, D.R. (2004). CRC Handbook of Chemistry and Physics, 84th Edition Edited by David R. Lide (National Institute of Standards and Technology). CRC Press LLC: Boca Raton. 2003. 2616 pp. $139.95. ISBN 0-8493-0484-9. J. Am. Chem. Soc. *126*, 1586. https://doi.org/10.1021/ja0336372.
19. Kelsall, C.C. (2023). Design Challenges for Ultra-High-Temperature Energy Storage with Thermophotovoltaics (Massachusetts Institute of Technology).
20. Pawar, P., Ballav, R., and Kumar, A. (2017). Machining processes of silicon carbide: A review. Rev. Adv. Mater. Sci. *51*, 62–76.
21. Cui, K., Lemaire, P., Zhao, H., Savas, T., Parsons, G., and Hart, A.J. (2018). Tungsten–Carbon Nanotube Composite Photonic Crystals as Thermally Stable Spectral-Selective Absorbers and Emitters for Thermophotovoltaics. Adv. Energy Mater. *8*, 1801471. https://doi.org/10.1002/aenm.201801471.
22. Torres, J.F., Tsuda, K., Murakami, Y., Guo, Y., Hosseini, S., Asselineau, C.-A., Taheri, M., Drewes, K., Tricoli, A., Lipiński, W., et al. (2022). Highly efficient and durable solar thermal energy harvesting via scalable hierarchical coatings inspired by stony corals. Energy Environ. Sci. *15*, 1893–1906. https://doi.org/10.1039/D1EE03028K.
23. Bhatt, R., Kravchenko, I., and Gupta, M. (2020). High-efficiency solar thermophotovoltaic system using a nanostructure-based selective emitter. Sol. Energy *197*, 538–545. https://doi.org/10.1016/j.solener.2020.01.029.
24. Gong, T., Duncan, M.A., Karahadian, M., Leite, M.S., and Munday, J.N. (2023). Broadband Superabsorber Operating at 1500 °C Using Dielectric Bilayers. ACS Appl. Opt. Mater. *1*, 1615–1619. https://doi.org/10.1021/acsaom.3c00229.
25. Shklover, V., Braginsky, L., Witz, G., Mishrikey, M., and Hafner, C. (2008). High-temperature photonic structures. Thermal barrier coatings, infrared sources and other applications. J. Comp. Theor. Nanosci. *5*, 862–893. https://doi.org/10.1166/jctn.2008.2532.
26. Sakakibara, R., Stelmakh, V., Chan, W.R., Ghebrebrhan, M., Joannopoulos, J.D., Soljačić, M., and Čelanović, I. (2019). Practical emitters for thermophotovoltaics: a review. J. Photonics Energy *9*, 032713. https://doi.org/10.1117/1.JPE.9.032713.
27. Chandler, H.E. (1989). Machining of Refractory Metals. In ASM Handbook Machining, ASM Handbook Committee., ed. (ASM International), pp. 858–869. https://doi.org/10.31399/asm.hb.v16.a0002190.
28. Ordal, M.A., Bell, R.J., Alexander, R.W., Newquist, L.A., and Querry, M.R. (1988). Optical properties of Al, Fe, Ti, Ta, W, and Mo at submillimeter wavelengths. Appl. Opt. *27*, 1203–1209. https://doi.org/10.1364/AO.27.001203.
29. Liu, X., Coxon, P.R., Peters, M., Hoex, B., Cole, J.M., and Fray, D.J. (2014). Black silicon: fabrication methods, properties and solar energy applications. Energy Environ. Sci. *7*, 3223–3263. https://doi.org/10.1039/C4EE01152J.
30. Sani, E., Sciti, D., Silvestroni, L., Bellucci, A., Orlando, S., and Trucchi, D.M. (2020). Tailoring optical properties of surfaces in wide spectral ranges by multi-scale femtosecond-laser texturing: A case-study for TaB2 ceramics. Opt. Mater. *109*, 110347. https://doi.org/10.1016/j.optmat.2020.110347.
31. Chen, G., Xie, E., Zhao, Q., Ye, Z., Wang, S., Zou, Y., Wang, Y., Qiu, J., Ouyang, J., Wang, J., et al. (2024). Surface phonon activation for broadband high emissivity via textured structure on TiO2 coating. Appl. Surf. Sci. *673*, 160818. https://doi.org/10.1016/j.apsusc.2024.160818.
32. Amemiya, K., Shimizu, Y., Koshikawa, H., Shitomi, H., and Yamaki, T. (2023). Supreme-black levels enabled by touchproof microcavity surface texture on anti-backscatter matrix. Sci. Adv. *9*, eade4853. https://doi.org/10.1126/sciadv.ade4853.
33. Zhou, J., Chen, T.G., Tsurimaki, Y., Hajj-Ahmad, A., Fan, L., Peng, Y., Xu, R., Wu, Y., Assawaworrarit, S., Fan, S., et al. (2023). Angle-selective thermal emitter for directional radiative cooling and heating. Joule *7*, 2830–2844. https://doi.org/10.1016/j.joule.2023.10.013.

34. Bäuerle, D.W. (2011). Laser Processing and Chemistry, Fourth Edition (Springer). https://doi.org/10.1007/978-3-642-17613-5.

35. Zorba, V., Stratakis, E., Barberoglou, M., Spanakis, E., Tzanetakis, P., Anastasiadis, S.H., and Fotakis, C. (2008). Biomimetic Artificial Surfaces Quantitatively Reproduce the Water Repellency of a Lotus Leaf. Adv. Mater. *20*, 4049–4054. https://doi.org/10.1002/adma.200800651.

36. Long, J., Fan, P., Gong, D., Jiang, D., Zhang, H., Li, L., and Zhong, M. (2015). Superhydrophobic Surfaces Fabricated by Femtosecond Laser with Tunable Water Adhesion: From Lotus Leaf to Rose Petal. ACS Appl. Mater. Interfaces *7*, 9858–9865. https://doi.org/10.1021/acsami.5b01870.

37. Paeng, D., Yoo, J.-H., Yeo, J., Lee, D., Kim, E., Ko, S.H., and Grigoropoulos, C.P. (2015). Low-Cost Facile Fabrication of Flexible Transparent Copper Electrodes by Nanosecond Laser Ablation. Adv. Mater. *27*, 2762–2767. https://doi.org/10.1002/adma.201500098.

38. Kerse, C., Kalaycıoğlu, H., Elahi, P., Çetin, B., Kesim, D.K., Akçaalan, Ö., Yavaş, S., Aşık, M.D., Öktem, B., Hoogland, H., et al. (2016). Ablation-cooled material removal with ultrafast bursts of pulses. Nature *537*, 84–88. https://doi.org/10.1038/nature18619.

39. Chichkov, B.N., Momma, C., Nolte, S., von Alvensleben, F., and Tünnermann, A. (1996). Femtosecond, picosecond and nanosecond laser ablation of solids. Appl. Phys. A *63*, 109–115. https://doi.org/10.1007/BF01567637.

40. Guay, J.-M., Calà Lesina, A., Côté, G., Charron, M., Poitras, D., Ramunno, L., Berini, P., and Weck, A. (2017). Laser-induced plasmonic colours on metals. Nat. Commun. *8*, 16095. https://doi.org/10.1038/ncomms16095.

41. Vorobyev, A.Y., and Guo, C. (2008). Colorizing metals with femtosecond laser pulses. Appl. Phys. Lett. *92*, 041914. https://doi.org/10.1063/1.2834902.

42. Siddiquie, R.Y., Gaddam, A., Agrawal, A., Dimov, S.S., and Joshi, S.S. (2020). Anti-Biofouling Properties of Femtosecond Laser-Induced Submicron Topographies on Elastomeric Surfaces. Langmuir *36*, 5349–5358. https://doi.org/10.1021/acs.langmuir.0c00753.

43. Kudryashov, S.I., Nguyen, L.V., Kirilenko, D.A., Brunkov, P.N., Rudenko, A.A., Busleev, N.I., Shakhmin, A.L., Semencha, A.V., Khmelnitsky, R.A., Melnik, N.N., et al. (2018). Large-Scale Laser Fabrication of Antifouling Silicon-Surface Nanosheet Arrays via Nanoplasmonic Ablative Self-Organization in Liquid CS_2 Tracked by a Sulfur Dopant. ACS Appl. Nano Mater. *1*, 2461–2468. https://doi.org/10.1021/acsanm.8b00392.

44. Jalil, S.A., Lai, B., ElKabbash, M., Zhang, J., Garcell, E.M., Singh, S., and Guo, C. (2020). Spectral absorption control of femtosecond laser-treated metals and application in solar-thermal devices. Light Sci. Appl. *9*, 14. https://doi.org/10.1038/s41377-020-0242-y.

45. Reicks, A., Tsubaki, A., Anderson, M., Wieseler, J., Khorashad, L.K., Shield, J.E., Gogos, G., Alexander, D., Argyropoulos, C., and Zuhlke, C. (2021). Near-unity broadband omnidirectional emissivity via femtosecond laser surface processing. Commun. Mater. *2*, 36. https://doi.org/10.1038/s43246-021-00139-w.

46. Liu, Z., Hu, Z., Qi, J., Li, C., Wang, Y., Qian, M., and Liu, X. (2024). Fabrication of black metal surface for high solar energy absorption by femtosecond laser hybrid technology. Opt. Express *32*, 38655–38667. https://doi.org/10.1364/OE.537096.

47. Vorobyev, A.Y., and Guo, C. (2010). Metallic Light Absorbers Produced by Femtosecond Laser Pulses. Adv. Mech. Eng. *2*, 452749. https://doi.org/10.1155/2010/452749.

48. Wen, Z., Cai, S., Zhang, Z., Xu, Z., Song, Q., Zhang, K., Li, M., Shi, H., Hou, Y., and Zhang, Z. (2022). Dual-Scale Textured Broadband Si-Based Light Absorber. Nanomaterials (Basel) *12*, 4285. https://doi.org/10.3390/nano12234285.

49. Shen, X., Yang, L., Fan, S., Yang, Q., Wu, W., and Zhang, B. (2020). Colorful and superhydrophobic titanium surfaces textured by obliquely incident femtosecond laser induced micro/nano structures. Opt. Commun. *466*, 125687. https://doi.org/10.1016/j.optcom.2020.125687.

50. Jung, W., Kim, H., Mishchik, K., Lee, K., Ryu, J., Lee, S.J., Jeong, S.H., and Roh, C.L. (2024). Direct laser patterning of glass mask for micro display using GHz bursts. J. Soc. Inf. Disp. *32*, 426–434. https://doi.org/10.1002/jsid.1308.

51. Park, M., Grbčić, L., Motameni, P., Song, S., Singh, A., Malagrino, D., Elzouka, M., Vahabi, P.H., Todeschini, A., de Jong, W.A., et al. (2024). Inverse Design of Photonic Surfaces via High throughput Femtosecond Laser Processing and Tandem Neural Networks. Adv. Sci. (Weinh) *11*, e2401951. https://doi.org/10.1002/advs.202401951.

52. Park, J.H., Pattipaka, S., Hwang, G.-T., Park, M., Woo, Y.M., Kim, Y.B., Lee, H.E., Jeong, C.K., Zhang, T., Min, Y., et al. (2024). Light–Material Interactions Using Laser and Flash Sources for Energy Conversion and Storage Applications. Nano Micro Lett. *16*, 276. https://doi.org/10.1007/s40820-024-01483-5.

53. Wen, C.-D., and Mudawar, I. (2006). Modeling the effects of surface roughness on the emissivity of aluminum alloys. Int. J. Heat Mass Transf. *49*, 4279–4289. https://doi.org/10.1016/j.ijheatmasstransfer.2006.04.037.

54. Park, M., Gu, Y., Mao, X., Grigoropoulos, C.P., and Zorba, V. (2023). Mechanisms of ultrafast GHz burst fs laser ablation. Sci. Adv. *9*, eadf6397. https://doi.org/10.1126/sciadv.adf6397.

55. Park, M., Jeun, J., Han, G., and Grigoropoulos, C.P. (2020). Time-resolved emission and scattering imaging of plume dynamics and nanoparticle ejection in femtosecond laser ablation of silver thin films. Appl. Phys. Lett. *116*, 234105. https://doi.org/10.1063/5.0009227.

56. Martínez, N., Lopez-Herraiz, M., Rico, A., Múnez, C.J., and Poza, P. (2023). Influence of different thermal degradation processes on the optical property of Pyromark-2500. Sol. Energy *253*, 58–72. https://doi.org/10.1016/j.solener.2023.02.004.

57. Oehrlein, G.S. (1986). Reactive-Ion Etching. Phys. Today *39*, 26–33. https://doi.org/10.1063/1.881066.

58. McGinnity, T.L., Dominguez, O., Curtis, T.E., Nallathamby, P.D., Hoffman, A.J., and Roeder, R.K. (2016). Hafnia (HfO_2) nanoparticles as an X-ray contrast agent and mid-infrared biosensor. Nanoscale *8*, 13627–13637. https://doi.org/10.1039/C6NR03217F.

59. Franke, E., Schubert, M., Trimble, C.L., DeVries, M.J., and Woollam, J.A. (2001). Optical properties of amorphous and polycrystalline tantalum oxide thin films measured by spectroscopic ellipsometry from 0.03 to 8.5 eV. Thin Solid Films *388*, 283–289. https://doi.org/10.1016/S0040-6090(00)01881-2.

60. Datas, A., Ramos, A., Martí, A., del Cañizo, C., and Luque, A. (2016). Ultra high temperature latent heat energy storage and thermophotovoltaic energy conversion. Energy *107*, 542–549. https://doi.org/10.1016/j.energy.2016.04.048.

61. Mustafa, K.F., Abdullah, S., Abdullah, M.Z., and Sopian, K. (2017). A review of combustion-driven thermoelectric (TE) and thermophotovoltaic (TPV) power systems. Renew. Sustain. Energy Rev. *71*, 572–584. https://doi.org/10.1016/j.rser.2016.12.085.

62. Chan, W., Huang, R., Wang, C., Kassakian, J., Joannopoulos, J., and Celanovic, I. (2010). Modeling low-bandgap thermophotovoltaic diodes for high-efficiency portable power generators. Sol. Energy Mater. Sol. Cells *94*, 509–514. https://doi.org/10.1016/j.solmat.2009.11.015.

63. Zhao, B., Chen, K., Buddhiraju, S., Bhatt, G., Lipson, M., and Fan, S. (2017). High-performance near-field thermophotovoltaics for waste heat recovery. Nano Energy *41*, 344–350. https://doi.org/10.1016/j.nanoen.2017.09.054.

64. Lu, Q., Zhou, X., Krysa, A., Marshall, A., Carrington, P., Tan, C.-H., and Krier, A. (2018). InAs thermophotovoltaic cells with high quantum efficiency for waste heat recovery applications below 1000 °C. Sol. Energy Mater. Sol. Cells *179*, 334–338. https://doi.org/10.1016/j.solmat.2017.12.031.

65. LaPotin, A.D. (2024). Characterization of Thermophotovoltaics and Materials for High-Temperature Thermal Energy Storage (Massachusetts Institute of Technology).

66. Tervo, E.J., France, R.M., Friedman, D.J., Arulanandam, M.K., King, R.R., Narayan, T.C., Luciano, C., Nizamian, D.P., Johnson, B.A., Young, A.R., et al. (2022). Efficient and scalable GaInAs thermophotovoltaic devices. Joule *6*, 2566–2584. https://doi.org/10.1016/j.joule.2022.10.002.

67. Dias, M.R.S., Gong, T., Duncan, M.A., Ness, S.C., McCormack, S.J., Leite, M. S., and Munday, J.N. (2023). Photonics roadmap for ultra-high-temperature thermophotovoltaics. Joule *7*, 2209–2227. https://doi.org/10.1016/j.joule.2023.08.015.

68. Roy-Layinde, B., Lim, J., Arneson, C., Forrest, S.R., and Lenert, A. (2024). High-efficiency air-bridge thermophotovoltaic cells. Joule *8*, 2135–2145. https://doi.org/10.1016/j.joule.2024.05.002.

69. Verma, S., Buznitsky, K., and Henry, A. (2024). Thermophotovoltaic performance metrics and technoeconomics: efficiency vs. power density. Appl. Energy *384*, 125479.

70. Ambrosini, A., Boubault, A., Ho, C.K., Banh, L., and Lewis, J.R. (2019). Influence of application parameters on stability of Pyromark® 2500 receiver coatings. AIP Conf. Proc. *2126*, 030002. https://doi.org/10.1063/1.5117514.

71. Rubin, E.B., Chen, Y., and Chen, R. (2019). Optical properties and thermal stability of Cu spinel oxide nanoparticle solar absorber coatings. Sol. Energy Mater. Sol. Cells *195*, 81–88. https://doi.org/10.1016/j.solmat.2019.02.032.

72. Noč, L., Šest, E., Kapun, G., Ruiz-Zepeda, F., Binyamin, Y., Merzel, F., and Jerman, I. (2019). High-solar-absorptance CSP coating characterization and reliability testing with isothermal and cyclic loads for service-life prediction. Energy Environ. Sci. *12*, 1679–1694. https://doi.org/10.1039/C8EE03536A.

73. Chirumamilla, M., Krishnamurthy, G.V., Knopp, K., Krekeler, T., Graf, M., Jalas, D., Ritter, M., Störmer, M., Petrov, A.Y., and Eich, M. (2019). Metamaterial emitter for thermophotovoltaics stable up to 1400 °C. Sci. Rep. *9*, 7241. https://doi.org/10.1038/s41598-019-43640-6.

74. Rinnerbauer, V., Yeng, Y.X., Chan, W.R., Senkevich, J.J., Joannopoulos, J. D., Soljačić, M., and Celanovic, I. (2013). High-temperature stability and selective thermal emission of polycrystalline tantalum photonic crystals. Opt. Express *21*, 11482–11491. https://doi.org/10.1364/OE.21.011482.

75. Chou, J.B., Yeng, Y.X., Lee, Y.E., Lenert, A., Rinnerbauer, V., Celanovic, I., Soljačić, M., Fang, N.X., Wang, E.N., and Kim, S.-G. (2014). Enabling Ideal Selective Solar Absorption with 2D Metallic Dielectric Photonic Crystals. Adv. Mater. *26*, 8041–8045. https://doi.org/10.1002/adma.201403302.

76. Chang, C.-C., Kort-Kamp, W.J.M., Nogan, J., Luk, T.S., Azad, A.K., Taylor, A.J., Dalvit, D.A.R., Sykora, M., and Chen, H.-T. (2018). High-Temperature Refractory Metasurfaces for Solar Thermophotovoltaic Energy Harvesting. Nano Lett. *18*, 7665–7673. https://doi.org/10.1021/acs.nanolett.8b03322.

77. Arpin, K.A., Losego, M.D., Cloud, A.N., Ning, H., Mallek, J., Sergeant, N.P., Zhu, L., Yu, Z., Kalanyan, B., Parsons, G.N., et al. (2013). Three-dimensional self-assembled photonic crystals with high temperature stability for thermal emission modification. Nat. Commun. *4*, 2630. https://doi.org/10.1038/ncomms3630.

78. Chirumamilla, M., Krishnamurthy, G.V., Rout, S.S., Ritter, M., Störmer, M., Petrov, A.Y., and Eich, M. (2020). Thermal stability of tungsten based metamaterial emitter under medium vacuum and inert gas conditions. Sci. Rep. *10*, 3605. https://doi.org/10.1038/s41598-020-60419-2.

79. Yeng, Y.X., Ghebrebrhan, M., Bermel, P., Chan, W.R., Joannopoulos, J.D., Soljačić, M., and Celanovic, I. (2012). Enabling high-temperature nanophotonics for energy applications. Proc. Natl. Acad. Sci. USA *109*, 2280–2285. https://doi.org/10.1073/pnas.1120149109.

80. Narayan, T.C., Nizamian, D.P., Luciano, C., Johnson, B.A., Limpinsel, M., Young, A.R., Briggs, J.A., Kuritzky, L.Y., Ponec, A.J., and Perl, E.E. (2021). Platform for accurate efficiency quantification of> 35% efficient thermophotovoltaic cells. 2021 IEEE 48th Photovoltaic Specialists Conference, PVSC 2021 (IEEE), 1352–1354.

81. López, E., Artacho, I., and Datas, A. (2023). Thermophotovoltaic conversion efficiency measurement at high view factors. Sol. Energy Mater. Sol. Cells *250*, 112069. https://doi.org/10.1016/j.solmat.2022.112069.